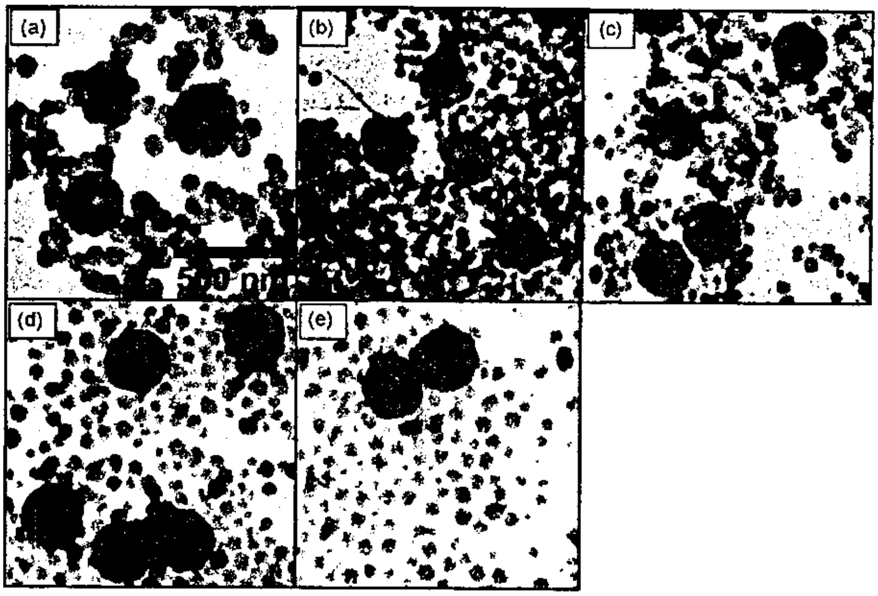

Fig. 3. TEM images of fluorescence microspheres coated with silica for 10.9 M water, 0.4 M ammonia and 0.02 M TEOS at PVP concentrations of (a) 0 g/l, (b) 0.01 g/l, (c) 0.1 g/l, (d) 1.0 g/l and (e) 10 g/l.

silica particles were still observed in Fig. 3(c). The surfaces of silica shell were smoother with the increase in PVP concentration. In our research, it can be considered that PVP improved an affinity between the silica nuclei and the fluorescent microsphere surfaces.

3.2. *Effect of water concentration*

Fig. 4 shows TEM micrographs of silica-coated fluorescent microspheres prepared at various water concentrations. In Fig. 4(a)–(c), homogeneous silica shells were observed on the surfaces of the fluorescent microspheres and their thickness increased from 13 to 60 nm with the water concentration. As Bogush and Zukoski reported [26], an increase in water concentration in TEOS/NH$_3$/water/ethanol solution dissociates ammonium hydroxide and brings about an increase in electric conductivity that corresponds to ionic strength. Since the increase in ionic strength reduces electrostatic repulsion between particles, the growth of silica shells was probably promoted.

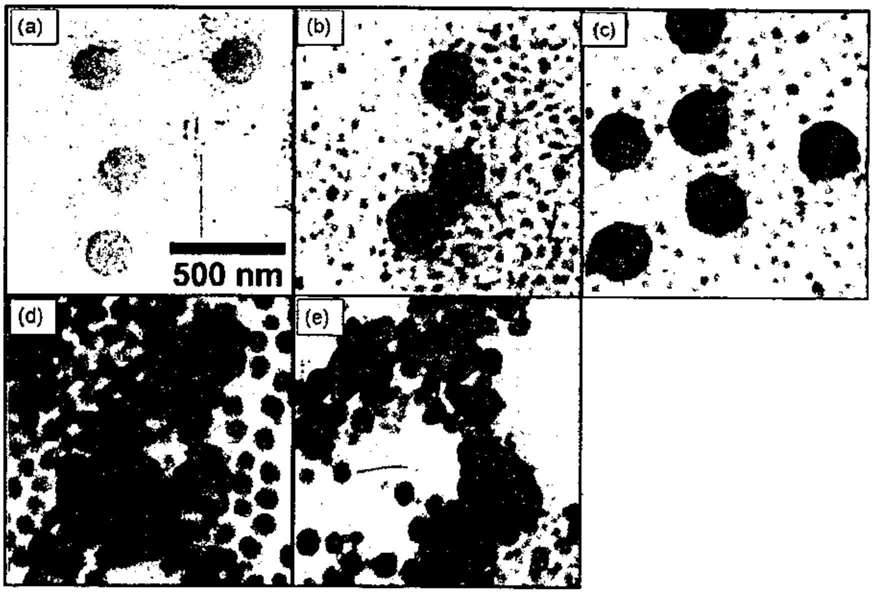

Fig. 4. TEM images of fluorescence microspheres coated with silica for 10 g/l PVP, 0.4 M ammonia and 0.02 M TEOS at initial water concentrations of (a) 1.13 M, (b) 5.0 M, (c) 10.9 M, (d) 13.0 M and (e) 17 M.

Many core-free silica particles were also observed and their average sizes increased from 41 to 92 nm with the water concentration. In Fig. 4(d) and (e), such silica particles adhered to the fluorescent microsphere surfaces and no more homogeneous shell was observed, which can not be explained by the change in ionic strength that was the factor causing the silica shell growth as shown in Fig. 4(a)–(c). Because the dielectric constant of water/ethanol mixture increases with water concentration, silanol groups on the silica particle surface probably tend to ionize with increasing water concentration. This might increase affinity of the silica particles for the dispersant. Therefore, silica nuclei generated during the early stages of the sol–gel reaction probably grew as stable core-free silica particles.

3.3. Effect of ammonia concentration

Fig. 5 shows TEM micrographs of silica-coated fluorescent microspheres prepared at different ammonia concentrations. At an ammonia concentration of 0 M (Fig. 5(a)), no silica shell and no silica particle was observed because of a shortage of catalyst. At ammonia concentrations of 0.2–0.8 M (Fig. 5(b)–(d)), the thickness of silica shell increased from 38 to 43 nm with the increase in ammonia concentration. Addition of ammonia increases the ionic strength of the solution and catalyzes the hydrolysis and condensation of the alkoxysilanes [27]. Thus, the high ammonia concentration should reduce the double layer repulsion between the fluorescent microspheres and the silica nuclei. As a result, the silica shells grew on the microsphere surfaces. At an ammonia concentration as high as 1.2 M, the fluorescent microspheres aggregated with the secondary generated silica particles (Fig. 5(e)). The high ammonia concentration extensively accelerated the sol–gel reaction of TEOS and then the core-free silica particles were generated from the silica nuclei and grew much before the silica nuclei was used for the silica shell formation.

3.4. Effect of TEOS concentration

Fig. 6 shows TEM micrographs of silica-coated fluorescent microspheres formed at various TEOS concentrations. Some silica particles were observed and their size tended to increase with the TEOS concentration. The ionic strength decreases as a sol–gel reaction of TEOS proceeds and then secondary silica particles are generated [28,29]. Since the high TEOS concentration should increase a source of silica, the silica shell grew. The silica shell thickness was varied from 13 to 138 nm as initial TEOS concentration increased from 0.00038 to 0.2 M. This means the shell thickness can be controlled within a certain threshold. The thickness of silica was smaller than those estimated from initial TEOS concentrations, because of the generation of the core-free silica particles.

3.5. Photo-bleaching

Fig. 7 shows the time-dependence of the fluorescence intensity. The fluorescence intensity of the silica-coated fluorescent microspheres was lower than that of the uncoated ones up to 15 min. However, the laser-irradiation over 15 min reversed the order of the fluorescence intensites. For making clear a difference between the silica-coated microspheres and the uncoated ones, the fluorescence intensities were normalized by the value of fluorescence intensity measured before the laser-irradiation, as shown in

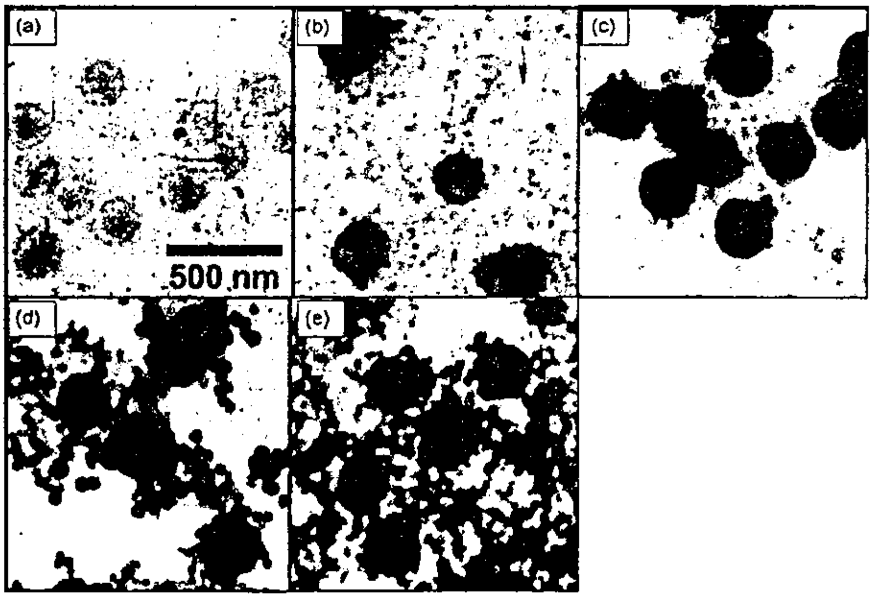

Fig. 5. TEM images of fluorescence microspheres coated with silica for 10 g/l PVP, 10.9 M water and 0.02 M TEOS at initial ammonia concentrations of (a) 0 M, (b) 0.2 M, (c) 0.4 M, (d) 0.8 M and (e) 1.2 M.

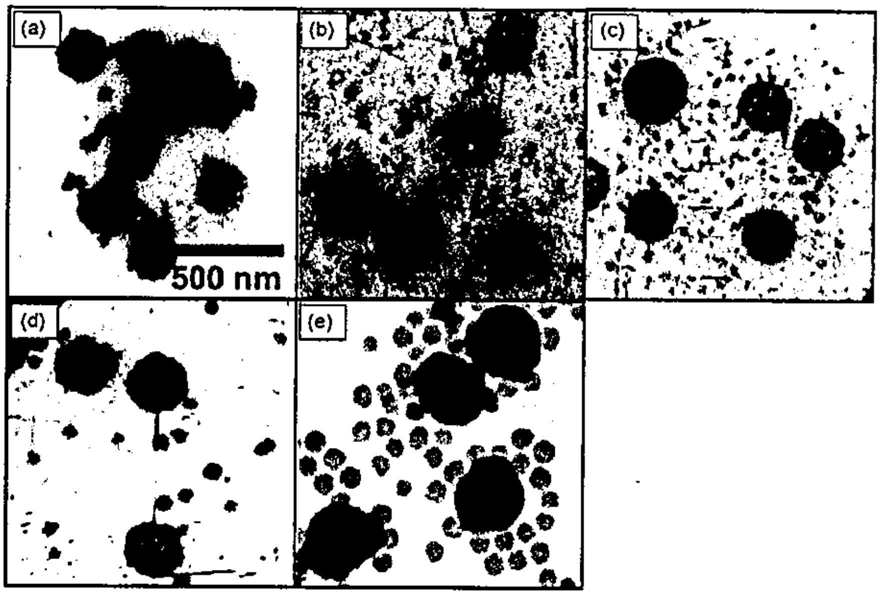

Fig. 6. TEM images of fluorescence microspheres coated with silica for 10 g/l PVP, 10.9 M water and 0.4 M ammonia at initial TEOS concentrations of (a) 0.00038 M, (b) 0.0015 M, (c) 0.009 M, (d) 0.02 M and (e) 0.2 M.

the inset. Time-dependence of the normalized fluorescence intensity for the silica-coated fluorescent microspheres was weak compared to that of the uncoated fluorescent microspheres, which is evidence that the silica-coated fluorescent microspheres were more stable in respect to their luminescence property than the uncoated ones. Singlet state oxygen molecules decompose dye molecules in their exited stage. [5–7]. This stable fluorescence property is probably related to the diffusional limitations of oxygen molecules inside of the fluorescent microspheres through the silica shell. Such stabilization by the silica-coating will be of importance in the preparation of stable materials for practical applications.

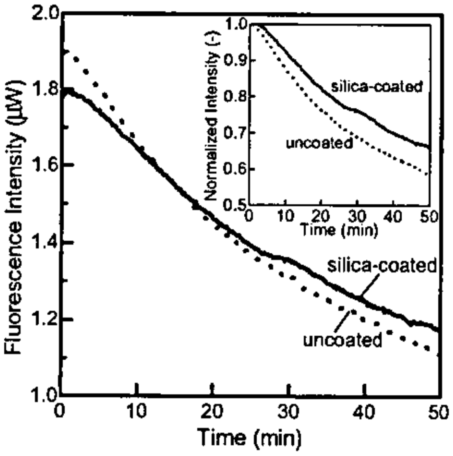

Fig. 7. Fluorescence intensities of silica-coated fluorescent microspheres and uncoated ones as a function of laser-irradiation time. The silica-coating was employed at 10 g/l PVP, 10.9 M water, 0.4 M ammonia and 0.02 M TEOS. The inset shows fluorescence intensity normalized by the value of fluorescence intensity measured before the laser-irradiation.

4. Conclusion

A synthetic method was developed for the stabilization of fluorescent microspheres. The method was based on the deposition of a silica shell on the fluorescent microsphere cores. The silica-coating was performed with a sol–gel reaction of TEOS in the presence of PVP and the fluorescent microspheres. Homogeneous silica shells were formed on the fluorescent microspheres in the presence of PVP. At high water and ammonia concentrations, no formation of homogeneous silica shells could be performed. With increasing TEOS concentration, the silica shell thickness increased. Concentration effects can probably be explained by differences in ionic strength of the solution. It was observed that the silica-coated fluorescent microspheres provided high luminescence stability, compared with uncoated ones. This property is significant for biomedical application.

Acknowledgements

This research was partially supported by the Ministry of Education, Culture, Sports, Science and Technology of Japan (Grant-in-Aid for the COE Project, Giant Molecules and Complex Systems), and by the Ministry of Health, Labor and Welfare of Japan.

References

[1] D.A.A. Vignali, J. Immunol. Methods 243 (2000) 243.
[2] M. Altun, E. Bergman, B. Ulfhake, J. Neurosci. Methods 108 (2001) 19.
[3] K.L. Kellar, M. Iannone, Exp. Hematol. 20 (2002) 1227.

[4] G. De Visscher, M. Haseldonckx, W. Flameng, M. Borgers, R.S. Reneman, K. van Rossem, J. Neurosci. Methods 122 (2003) 149.
[5] T. Suratwala, Z. Gardlund, K. Davidson, D.R. Uhlmann, S. Bonilla, N. Peyghambarian, J. Sol–Gel Sci. Technol. 8 (1997) 953.
[6] S. Singh, V.R. Kanetkar, G. Sridhar, V. Muthuswamy, K. Raja, J. Lumin. 101 (2003) 285.
[7] G. Qian, Y. Yang, Z. Wang, C. Yang, Z. Yang, M. Wang, Chem. Phys. Lett. 368 (2003) 555.
[8] F. Caruso, A.S. Susha, M. Giersig, H. Möhwald, Adv. Mater. 11 (1999) 950.
[9] F.G. Aliev, M.A. Correa-Duarte, A. Mamedov, J.W. Ostrander, M. Giersig, L.M. Liz-Marzán, N.A. Kotov, Adv. Mater. 11 (1999) 1006.
[10] J.-I. Park, J. Cheon, J. Am. Chem. Soc. 123 (2001) 5743.
[11] M. Wu, Y.D. Zhang, S. Hui, T.D. Xiao, S. Ge, W.A. Hines, J.I. Budnick, J. Appl. Phys. 92 (2002) 491.
[12] Y. Lu, Y. Yin, B.T. Mayers, Y. Xia, Nano Lett. 2 (2002) 183.
[13] S.M. Marinakos, D.A. Shultz, D.L. Feldheim, Adv. Mater. 11 (1999) 34.
[14] G. Oldfield, T. Ung, P. Mulvaney, Adv. Mater. 12 (2000) 1519.
[15] L.Y. Wang, Y.-J. Lin, W.-Y. Chiu, Synth. Met. 119 (2001) 155.
[16] H. Shiho, N. Kawahashi, Colloid Polym. Sci. 279 (2001) 1231.
[17] L.M. Liz-Marzán, M. Giersig, P. Mulvaney, Langmuir 12 (1996) 4329.
[18] M.A. Correa-Duarte, M. Giersig, L.M. Liz-Marzán, Chem. Phys. Lett. 286 (1998) 497.
[19] A. Rogach, A. Susha, F. Caruso, G. Sukhorukov, A. Kornowski, S. Kershaw, H. Möhwald, A. Eychmüller, H. Weller, Adv. Mater. 12 (2000) 333.
[20] M.A. Correa-Duarte, M. Giersig, L.M. Liz-Marzán, Chem. Phys. Lett. 286 (1998) 497.
[21] Y. Kobayashi, M. Horie, M. Konno, B. Rodríguez-González, L.M. Liz-Marzán, J. Phys. Chem. B 107 (2003) 7420.
[22] E. Mine, A. Yamada, Y. Kobayashi, M. Konno, L.M. Liz-Marzán, J. Colloid Interface Sci. 264 (2003) 365.
[23] H. Shiho, N. Kawahashi, J. Mater. Chem. 10 (2000) 2294.
[24] H. Shiho, N. Kawahashi, J. Colloid Interface Sci. 226 (2000) 91.
[25] H. Shiho, N. Kawahashi, Colloid Polym. Sci. 278 (2000) 270.
[26] G.H. Bogush, C.F. Zukoski, J. Colloid Interface Sci. 142 (1991) 1.
[27] E. Mine, M. Konno, J. Chem. Eng. Jpn. 34 (2001) 545.
[28] D. Nagao, Y. Kon, T. Satoh, M. Konno, J. Chem. Eng. Jpn. 33 (2000) 468.
[29] D. Nagao, T. Satoh, M. Konno, J. Colloid Interface Sci. 232 (2000) 102.

Biophoton detection as a novel technique for cancer imaging

Motohiro Takeda,[1] Masaki Kobayashi,[2] Mariko Takayama,[3] Satoshi Suzuki,[2] Takanori Ishida,[1] Kohji Ohnuki,[1] Takuya Moriya[4] and Noriaki Ohuchi[1,5]

[1]Division of Surgical Oncology, [3]Division of Dermatology and [4]Division of Pathology, Tohoku University Graduate School of Medicine, 1-1 Seiryo-machi, Aoba-ku, Sendai 980-8574; and [2]Division of Electronics, Tohoku Institute of Technology, 35 Kasumi-cho, Yagiyama, Taihaku-ku, Sendai 982-8577

(Received February 16, 2004/Revised June 16, 2004/Accepted June 16, 2004)

Biophoton emission is defined as extremely weak light that is radiated from any living system due to its metabolic activities, without excitation or enhancement. We measured biophoton images of tumors transplanted in mice with a highly sensitive and ultra-low noise CCD camera system. Cell lines employed for this study were AH109A, TE4 and TE9. Biophoton images of each tumor were measured 1 week after carcinoma cell transplantation to estimate the tumor size at week 1 and the biophoton intensity. Some were also measured at 2 and 3 weeks to compare the biophoton distribution with histological findings. We achieved sequential biophoton imaging during tumor growth for the first time. Comparison of microscopic findings and biophoton intensity suggested that the intensity of biophoton emission reflects the viability of the tumor tissue. The size at week 1 differed between cell lines, and the biophoton intensity of the tumor was correlated with the tumor size at week 1 (correlation coefficient 0.73). This non-invasive and simple technique has the potential to be used as an optical biopsy to detect tumor viability. (Cancer Sci 2004; 95: 656–661)

Ultraweak biophoton emission is defined as extremely weak light originating from living things as a result of their metabolic activities. This phenomenon has been recognized to occur without enhancement or excitement by chemical administration or light irradiation. Ultraweak biophoton emission ranges from the ultraviolet to the near infrared, and its intensity is generally lower than 10^{-9} W/cm^2, i.e., less than 1/1000 of the human visible light intensity.

Many living systems have been shown to exhibit biophoton emission since the invention of photo-multiplier tubes,[1] including proliferating *Saccharomyces cerevisiae*, longitudinal sections of bamboo shoot, injured soybean seedlings and fertilizing sea urchins.[2–5] All the results are consistent with pathological or physiological significance of biophoton emission. Samples from human beings, including smoker's breath and serum, also exhibit ultraweak light emission.[6] Thus, biophoton emission may be an indicator of pathological conditions in patients.

Cancer is a major cause of human mortality, and many diagnostic methods have been developed. Trials on ultraweak biophoton measurement of the serum or urine from cancer patients have also been performed for diagnostic applications.[7,8] Elevation of ultraweak light intensity from serum or urine has been attributed to metabolic changes in patients. Thus, measurement of carcinoma lesions might provide more accurate information on the pathological status of cancer. Shimizu *et al.* measured biophoton intensity from transplanted malignant tumors[9] and observed differences among the tumors, and Amano *et al.* presented biophoton images of bladder cancer transplanted in nude mice.[10] Although these results suggest the feasibility of biophoton measurement for cancer diagnosis, there has been no report discussing applications based on specific pathological features for cancer diagnosis.

In a recent study, we detected changes in biophoton emission from proliferating carcinoma cell cultures using a flow culture system coupled with a highly sensitive apparatus.[11] In the present study, TE9, an esophageal carcinoma cell line, exhibited quite similar changes in biophoton intensity during cell proliferation, and we measured the specific biophoton spectrum of a cell culture for the first time. The results demonstrated the applicability of biophoton measurement to the detection of cell proliferation for cancer diagnosis. Growth rate is one of the most important of the factors that define malignancy, and the results lead to the idea that biophoton emission may reflect the growth potential of the tumor.

In the present study, we investigated the relationship between biophoton intensity and tumor size after 1 week to ascertain the relationship of biophoton properties with the tumor growth potential. Furthermore, we took weekly measurements of the biophoton images of 3 different types of tumor for 2 or 3 weeks and compared them with the tumor histology to clarify the relationship between tissue distribution and the two-dimensional biophoton emission image. The feasibility of specific application of biophoton imaging is discussed.

Materials and Methods

Instrumentation. For the imaging of ultraweak light emission, a cooled charge-coupled device (CCD) camera system (ATC200C, Photometrics, Inc.) was utilized. A back-illuminated type of CCD (TK1024AB2, Tektronix, Inc.) is incorporated in the camera system with cooling at −120°C using liquid nitrogen. The camera head is mounted on a completely light-tight chamber, which includes a temperature-controlled mounting bed to maintain the body temperature of a mouse (Fig. 1).[12] A lens system (Nikor F/1.2, Nikon) was used for imaging an observation area measuring 100×100 mm. The CCD has a spectral sensitivity over the wavelength range from 400 to 1000 nm with a maximum quantum efficiency of 73% at 700 nm. Pixel size of the CCD is 24×24 μm with 1024×1024 format. In the experiments, the CCD camera was operated in 2×2 binning mode, with a resulting spatial resolution of 48×48 μm, which corresponded to a resolution of 190 μm on the object. Integration time for each measurement was 1 h. The minimum detectable intensity of the emission on a sample surface under the above condition is estimated to be 1.0×10^4 photons/s/cm^2, taking into account read-out noise and the dark current of the CCD, and the total light detection efficiency of the system. One count of the intensity indicated in figures corresponds to 1.64×10^4 photons emitted on the surface.

Image processing was made based on grey scale images of tumors. The images in figures shown in this article were further modified by converting emission intensity to specific colors according to a color bar (Fig. 2). Image processing for elimination of background noise induced by high-energy particles was applied with threshold filtering. The average emission intensity in the total region of the tumor was evaluated after subtraction of

---

[5]To whom correspondence should be addressed. E-mail: noriaki-o@umin.ac.jp

Fig. 1. Schematic of the biophoton imaging system. The biophoton imaging system consists of a liquid nitrogen-cooled highly sensitive CCD camera system (ATC200C, Photometrics), a completely light-shielded sample chamber, a thermostat heater to warm the mice, and a set of computers. The CCD camera system includes a back-illuminated, thinned type Si-CCD (TK1024AB2-G1, Tektronix). The CCD format is 1024×1024 pixels for a full frame, with each pixel size being 24×24 μm. The dark current of the device is 0.225 e⁻/h pixel at −120°C in MPP (multipinned phase) mode and the readout noise is 3.3 e⁻RMS/pixel.

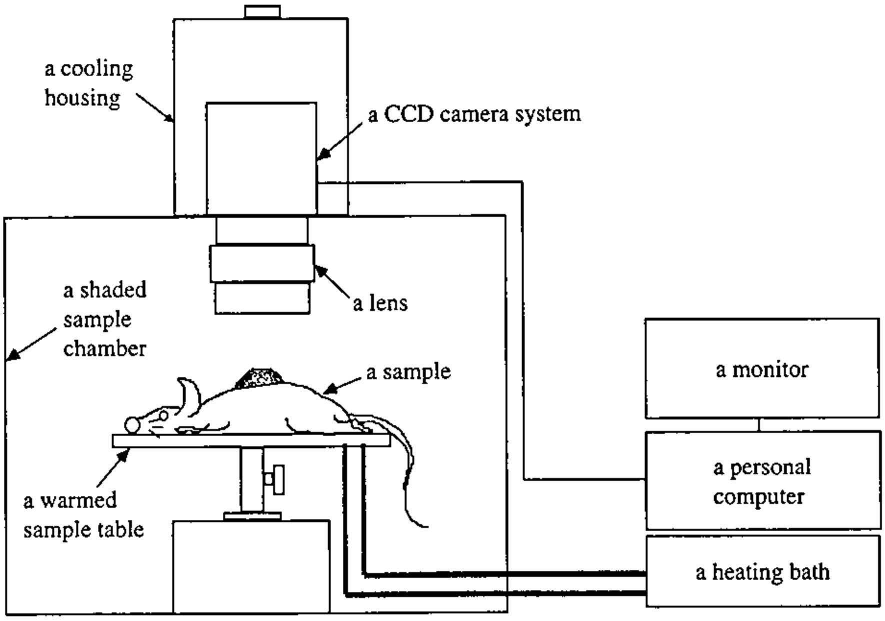

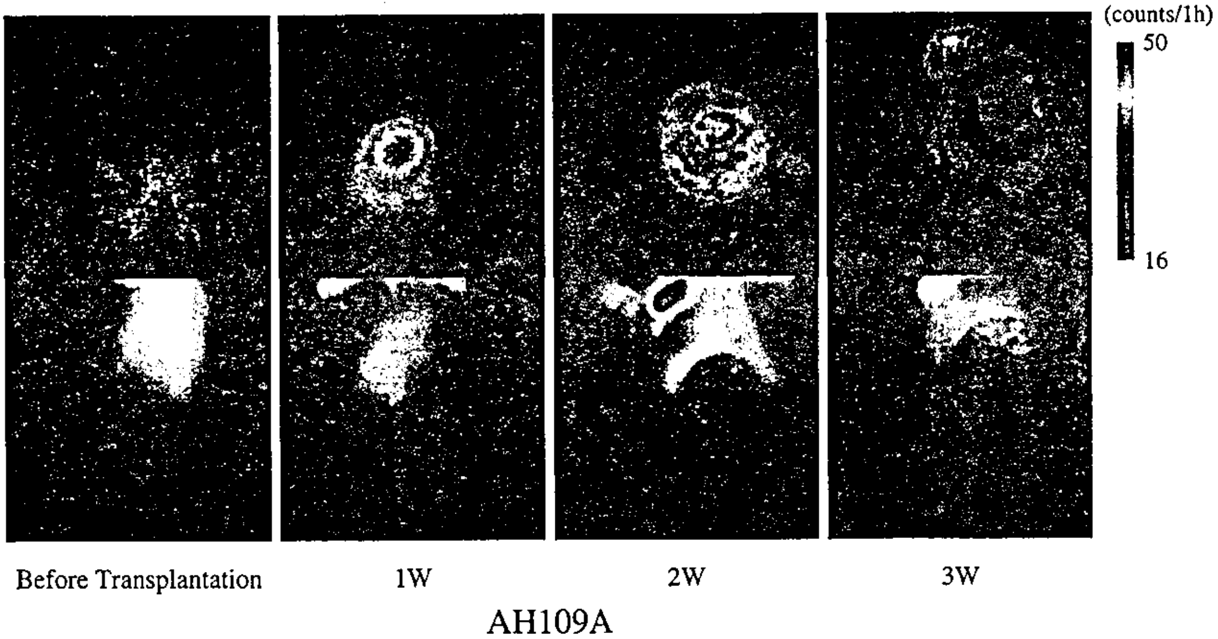

Fig. 2. Biophoton image and pathological findings of AH109A at week 1. The arrows drawn on the tumor corresponds to the cross-sectional line.

the background emission of the mouse determined at a circular region of 600–800 pixels between the blade bones, which exhibited good reproducibility with the lowest biophoton emission in the body of the mice.

Cell lines. The cell lines used in the present study were TE4, TE9 and AH109A. Both TE4 and TE9 are human esophageal carcinoma cell lines established in our department.[13] AH109A is a rat hepatoma cell line.[14] All of the cell lines were cultured in an RPMI1640 medium supplemented with 10% fetal bovine serum. The TE4 and TE9 cells were harvested for transplantation after detachment with trypsin and ethylenediaminetetraacetic acid (EDTA) when the cells were confluent on the bottom of the flasks. The AH109A cells proliferated as a suspension in the medium. The cell suspension was then centrifuged, and cells were collected for transplantation.

Chemicals and animals. We used RPMI1640 medium supplemented with 10% fetal bovine serum (FBS) without phenol red for cell culture. The RPMI1640 medium was purchased from Life Technologies, Inc. (Grand Island, NY) and the FBS was purchased from ICN, Inc. (Costa Mesa, CA). EDTA and trypsin were used to detach the cells from the bottom of the sample cuvettes and culture flasks. The EDTA was purchased from Life Technologies, Inc. and the trypsin was purchased from ICN, Inc. All chemicals were of culture grade.

Mice supplemented in this study were *nu/nu* male nude mice, 5–7 weeks old, purchased from Charles Liver, Inc.

Sample preparation and experimental details. Cells of each line (10^7 cells) were suspended in 0.1 ml of saline (cell volume 0.1

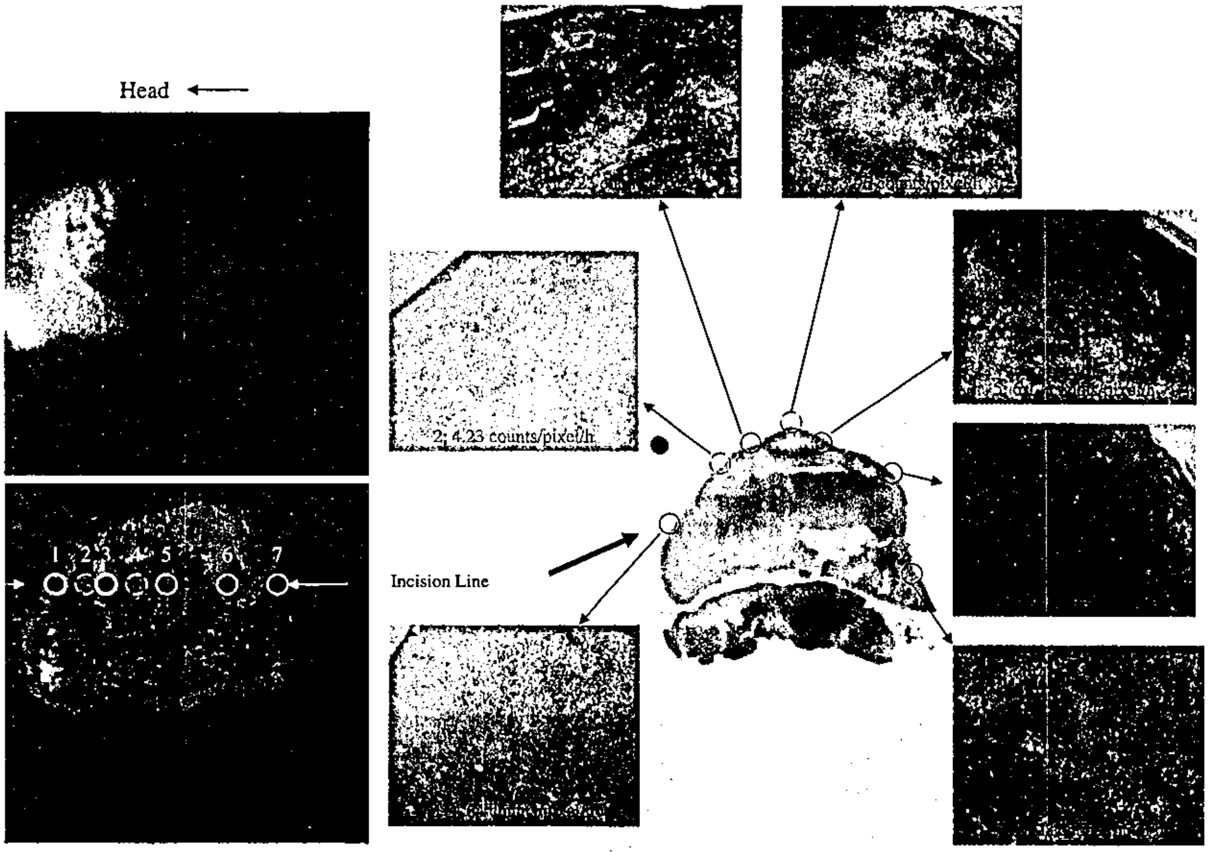

*solid line circles: live tissue, dotted line circles: necrotic tissue

Fig. 3. Changes in the ultraweak biophoton images with tumor growth. Ultraweak biophoton images taken after cell transplantation: week 1, week 2 and week 3.

ml) and 0.2 ml of cell suspension was injected subcutaneously into the backs of the nude mice. After transplantation, the mice were anesthetized with pentobarbital (0.05 mg/g) by intraperitoneal injection and fixed on a temperature-controlled sample table in a completely light-shielded sample chamber. Then biophoton imaging was performed for 1 h with detection of the raw image obtained by a biophoton detector under very weak illumination for estimation of tumor size. Thereafter, the mice were kept in their cages for 1 week and biophoton imaging was performed again for another hour. The correlation between tumor growth rate and biophoton intensity was made at week 1 because AH109A exhibited the fastest growth at that time point; at later times, tumor necrosis appears, and heterogeneity of growth occurs so that the growth rate cannot be properly estimated. Throughout the measurements, the body temperature of the mice was kept at about 37°C.

In some cases the nude mice were kept for 3 weeks for detection of ultraweak biophoton images and pathological examination. After biophoton imaging, the mice were sacrificed by cervical dislocation, and the tumors were excised and embedded in 10% buffered formalin for fixation. We sketched the shape of the tumor mass when we cut the sample for formalin fixation, and we compared the sketch of the pathological sample with the biophoton images. The measurement points of biophoton intensity were carefully identified. Comparison of the biophoton images and pathological slices revealed the relationship between the pathological findings and the two-dimensional biophoton images.

All animal experiments were approved by the Institutional Laboratory Animal Care and Use Committee of Tohoku University. All experiments were performed under UKCCCR guidelines (Workman *et al.*, 1998).[15]

Evaluation of growth rate and statistical analysis. Since the same numbers of cells in the same volume of 0.1 ml were introduced at the point of transplantation, we determined the size of tumors at week 1 to calculate the growth rate. The tumor size at week 1 was estimated from the product of the longest diameter and its perpendicular diameter. Tumor height was not measured at week 1 because the tumor was so thin that it was very difficult to measure.

Estimation of the tumor size and the emission intensity of biophoton images at week 1 were performed for 7 TE9 tumors, 9 TE4 tumors and 17 AH109A tumors. The emission intensity was measured by averaging the total tumor area with subtraction of background biophoton intensity obtained from the data measured at the midpoint of bilateral blade bones on the back of mice (this point exhibited the most stable biophoton intensity in the body throughout the measurement period).

The correlation coefficient was calculated from the biophoton intensity and tumor size (area) or square root of tumor size at week 1.

Biophoton intensity and tumor viability. To compare live and necrotic tumor, we observed 5 AH109A xenografts at 3 weeks. We classified each area into live or necrotic tissue, then we measured the biophoton intensity of corresponding circular areas of 697 pixels in biophoton images (Fig. 3). The intensity was measured in 40 live areas and 26 necrotic areas. Statistical analysis was done with a two tailed *t* test.

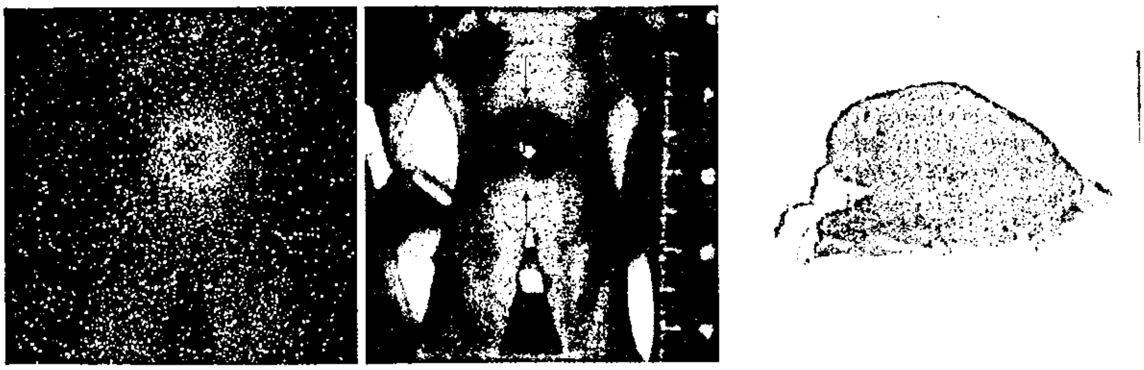

Biophoton Image Photograph Sample Slice with HE Stain

Fig. 4. Comparisons between biophoton image, raw image** and pathological findings of AH109A. An ultraweak biophoton image, raw image and histological images at week 1. The arrows drawn on the tumor corresponds to the cross-sectional line. ** The raw image taken under very weak illumination (3000–5000 photon counts/s) with the CCD camera used for the biophoton imagery.

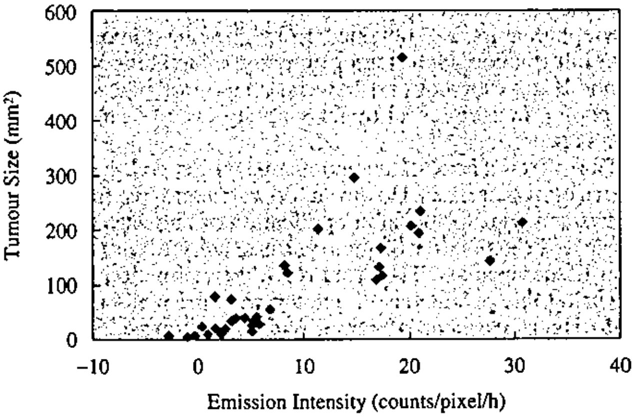

Fig. 5. Correlation between biophoton intensity and square root of tumor size at week 1. Tumor size and ultraweak biophoton intensity at the first week are plotted in the graph. The correlation coefficient of the tumor size at week 1 and ultraweak biophoton intensity is 0.73.

Results

Tumor growth and biophoton imaging. The tumors exhibited different growth modes for each cell line. Representative growth time courses and biophoton images are shown in Fig. 2. The rat hepatoma cell line AH109A showed the most rapid growth, reaching a size of about 700 mm^2 in 3 weeks. The human esophageal carcinoma cell line TE4 grew to the size of about 100 mm^2 in 3 weeks and the human esophageal carcinoma cell line TE9 grew to the size of about 40 mm^2 in a week, but shrank thereafter. The size of TE4 at week 1 was 24 mm^2.

The biophoton patterns also showed differences in each tumor cell strain. Although AH109A exhibited a homogeneous biophoton pattern at week 1, it exhibited a heterogeneous pattern after 2 weeks (Fig. 2). The emission intensity from TE4 was rather weak in the first week, but became more intense in weeks 2 and 3. The biophoton pattern from TE4 showed homogeneity until the third week. In contrast, TE9 showed very weak light emission; tumors were recognized as arising from the lower biophoton intensity area compared to neighboring normal tissue throughout the measurement period.

Nude mice showed specific biophoton emission related to internal organs and muscles in all measurements.

Comparisons of the biophoton pattern and surface appearance of the tumors showed distinct differences. In Fig. 3, part of the tumor showed high-intensity biophoton emission despite being covered with necrotic skin. In another area, the tumor showed low-intensity biophoton emission despite being covered with normal skin. Pathological findings suggest the area with high-intensity biophoton emission contains live tissue and the area with low-intensity biophoton emission contains necrotic tissue (Fig. 3).

Table 1. Comparison of tissue viability and biophoton intensity of AH109A

Tissue viability	Biophoton intensity	
Live tissue	2.93±3.34 1)	2)
Necrotic tissue	10.76±6.52 1)	

1) Photon counts/pixel/h.
2) P=2.30E-8.

Biophoton intensity and tumor growth rate. Pathological observation of AH109A at week 1 revealed homogeneous tissue (Fig. 4).

The average biophoton intensities of the TE9, TE4 and AH109A tumors at week 1 were 3.37±2.23, 2.42±3.09 and 13.55±8.40 counts/pixel/h, respectively. After 1 week, AH109A reached 167.1±55.1 mm^2, while TE9 grew to 41.4±18.7 mm^2 and TE4 grew to 24.1±12.7 mm^2. AH109A showed the highest emission intensity among all the tumors. The biophoton intensity of AH109A was significantly higher than those of TE9 and TE4 (P=0.0001 and P=0.00006, respectively). The P value between TE4 and TE9 was 0.49.

The relationship between biophoton intensity and tumor size at week 1 is shown in Fig. 5. The correlation coefficient of the biophoton intensity and tumor size at week 1 for all tumors was 0.73 and the correlation coefficient of the biophoton intensity and the square root of tumor size was 0.82.

Biophoton intensity and tumor viability. The emission intensity of living tissue, measured in 40 areas, amounted to 10.76±6.52 photon counts/pixel/h, and that of necrotic tissue measured in 26 areas was 2.93±3.34 photon counts/pixel/h. The P value was 0.00077 (Table 1).

Discussion

Although the biophoton images of the AH109A tumor exhibited homogeneous patterns at week 1, they exhibited heterogeneous patterns thereafter. This heterogeneity is not due to the surface condition of the skin, but reflects the viability of the underlying tumor tissue, as judged by microscopic observation.

TE4 grew to approximately 100 mm^2 in 3 weeks and the biophoton image exhibited a homogeneous pattern until the third week. Pathological findings of TE4 showed a homogeneous pattern in accord with the biophoton image.

The biophoton intensity of TE9 at week 1 was greater than that of TE4. TE9 exhibited an extremely weak biophoton intensity at week 3 that was lower than the emission intensity of TE4 or the normal tissue around the tumor. The growth pattern of TE9, i.e., reaching maximum size during week 1 and shrinking thereafter, is in agreement with the biophoton results. Pathological findings showed no vessel formation in TE9.

Although the biophoton images of TE4 and TE9 at week 1 cannot be easily differentiated from those of normal tissue at present, spectral analysis may be helpful for recognition of such tumors.[11]

The non-tumor regions in the nude mice showed specific biophoton patterns related to the organ distribution. The lumbar muscle and digestive organs showed enhanced biophoton emission. These phenomena suggest that studies to evaluate the relationship between physiological function and biophoton emission would be of value.

The growth rates and biophoton intensities of AH109A tumors are significantly higher than those of TE9 and TE4. Additionally, biophoton intensity and tumor size at week 1 were correlated, with a correlation coefficient of 0.73 (Fig. 5). This result suggests that ultraweak biophoton emission is related to growth activity, presumably via metabolic activity. Thus, we can argue that areas with high intensity of biophoton emission contain live tissue and have high-growth activity, while areas with low-intensity biophoton emission contain necrotic tissue or tissue with a very low-growth rate.

Biophoton emission has been attributed to oxidative metabolism in live organisms, and it was reported that electron leakage from mitochondria results in the generation of active oxygen species such as the superoxide anion, hydrogen peroxide, hydroxyl radical and singlet oxygen.[16] Oxidation of cellular molecules causes excitement of other fluorescent molecules that results in biophoton emission.[1, 17-19] In addition, cancer tissue contains fewer reactive oxygen quenchers than normal tissues, including superoxide dismutase (SOD) and catalase.[20] In normal tissue, reactive oxygen species are immediately eliminated by self-defence mechanisms consisting of SOD, catalase, vitamin E, glutathione, etc., in the cells. In morbid tissue, however, the balance between reactive oxygen generation and quenching activity is destroyed. Although the mechanism of this phenomenon is not clear at present, it is speculated that the relatively fast growth of malignant tumor generates a large amount of reactive oxygen species, leading to intense biophoton emission. The mechanism of this phenomenon should be examined.

Inflammation is also a cause of biophoton emission owing to active oxygen species from neutrophils, which generate singlet oxygen. Since singlet oxygen shows specific absorption at 703 nm, spectral analysis might be useful to distinguish malignant tissue from inflammation.

Tumor growth rate is one of the most important factors that define malignancy. No existing imaging modality except for positron emission tomography (PET) is able to evaluate metabolic activity. Our results suggest that biophoton measurement can detect growth activity, and it requires no isotope-labeled substrates, nor a cyclotron to prepare them, as is needed for PET. Biophoton measurement requires only a completely shielded space and compact detectors, requiring no chemical administration. Thus, biophoton measurement could be useful as a simple non-invasive method to obtain pathological information. PET is preferably used in screening of distant metastases or occult lesions of malignancies. Applications of biophoton measurement should be different from those of PET, because biophoton emission at the body surface represents light emission from only as deep as 3 mm from the tissue surface. Thus, biophoton measurement might be suitable for non-invasive sequential or repeated pathological diagnoses of recognized tumors but not for screening. For measurement of deeper tissue, a needle-coupled measurement probe would be needed. Biophoton measurements also have the advantage of being inexpensive.

This measurement technique may also be available for recognizing extremely thin tumors that are not palpable or visually apparent.

Image aquisition took 1 h in this study, and the measurement time should be shortened for clinical application. Recent development of measurement apparatus with high efficiency can shorten the image acquisition time, which is less than 30 min with the latest detector.

Biophoton images obtained from growing tumors can provide information about tumor properties, including whether the tumor is alive or not and how fast it is growing. In addition, biophoton images reveal tumor viability even when the surface skin is necrotic.

The effectiveness of chemotherapy is generally assessed in terms of tumor size. However, this standard parameter often shows a slow response after application of anticancer therapies, because the reduction of tumor size usually occurs much later than tissue necrosis. Therefore real-time estimation is impossible using this parameter. Biophoton measurements might allow real-time assessment of tumor viability through detection of changes in emission intensity.

In our study, necrotic areas showed low emission intensity in the heterogeneous mass. These results suggest that we can distinguish living area and necrotic area by biophoton measurement. Moreover, sequential measurement of biophoton emission during chemotherapy may enable us to detect tumor necrosis induced by chemotherapy. Because different chemotherapeutic agents have distinct mechanisms of action, characteristic changes of biophoton emission during the transition from the living state of the tumor to the necrotic state might be observable.

In conclusion, this method could be useful to assess not only malignancy, but also the efficacy of chemotherapy or radiotherapy in terms of viability, rather than tumor size. Although biophoton emission can be detected only on the body surface at present, deeper targets should be detected by the use of endoscopy or needle-coupled devices. This procedure may thus provide a non-invasive or minimally invasive optical biopsy as an adjunct to or replacement of existing diagnostic methods. We are now trying to detect other malignant xenografts to confirm the validity of this approach to measure tumor growth rate.

The authors thank Professor Kudo of the Medical Cell Storage Center, Institute of Aging, Tohoku University for providing the TE4, TE9 and AH109A cell lines. The authors declare that they have no competing financial interests.

1. Popp FA, Gurwitsch AA, Inaba H, Slawinski J, Cilento G, van Wijk R, Chwirot WB, Nagl W. Biophoton emission. *Experientia* 1988; **44**: 543–630.
2. Quickenden TI, Que Hee SS. Weak luminescence from the yeast *Saccharomyces cerevisiae* and the existence of mitogenetic radiation. *Biochem Biophys Res Commun* 1974; **60** (2): 764–70.
3. Totsune H, Nakano M, Inaba H. Chemiluminescence from bamboo shoot cut. *Biochem Biophys Res Commun* 1993; **194** (3): 1025–9.
4. Suzuki S, Usa M, Nagoshi T, Kobayashi M, Watanabe H, Inaba H. Two-dimensional imaging and counting of ultraweak emission patterns from injured plant seedlings. *J Photochem Photobiol B Biol* 1991; **9**: 211–7.

5. Takahashi A, Totsune-Nakano H, Nakano M, Mashiko S, Suzuki N, Ohma C, Inaba H. Generation of O_2^{-} and tyrosine cation-mediated chemiluminescence during the fertilization of sea urchin eggs. *FEBS Lett* 1989; **246**: 117–9.
6. Yoda B, Abe R, Goto Y, Saeki A, Takyu C, Inaba H. Spontaneous chemiluminescence of smoker's blood. In: Kricka LJ, Stanley PE, Thorp GHG, Whitehead TP, editors. Analytical applications of bioluminescence and chemiluminescence. Orlando, FL: Academic Press; 1984. p. 587–90.
7. Gisler GC, Diaz J, Duran N. Observation on blood plasma chemiluminescence in normal subjects and cancer patients. *Arq Biol Technol* 1983; **26** (3): 345–352.
8. Chilton CP, Rose GA. Urinary chemiluminescence-an evaluation of its use in clinical practice. *Br J Urol* 1984; **56**: 650–4.
9. Shimizu Y, Inaba H, Kumaki K, Mizuno K, Hata S, Tomita S. Measuring methods for ultra-low light intensity and their application to extra-weak spontaneous bioluminescence from living tissues. *IEEE Trans Instrum Meas* 1973; **IM-22**: 153–7.
10. Amano T, Kobayashi M, Devaraj B, Usa M, Inaba H. Ultraweak biophoton emission imaging of transplanted bladder cancer. *Urol Res* 1995; **23**: 315–8.
11. Takeda M, Tanno Y, Kobayashi M, Devaraj B, Usa M, Ohuchi N, Inaba H. A novel method of cancer cell proliferation by biophoton emission. *Cancer Lett* 1998; **127**: 155–60.
12. Kobayashi M, Devaraj B, Usa M, Tanno Y, Takeda M, Inaba H. Two-dimensional imaging of ultraweak photon emission from germinating soybean seedlings with a highly sensitive CCD camera. *Photochem Photobiol* 1997; **65** (3): 535–7.
13. Nishihira T, Katayama M, Hashimoto Y, Akaishi T. Cell lines from esophageal tumors. In: Atlas of human tumor cell lines. Academic Press Inc; 1994. p. 269–85.
14. Odashima S. Establishment of ascites .hepatoma in the rat, 1951–1963. Ascites tumors-Yoshida sarcoma and ascites hepatoma(s). *Natl Cancer Inst Monogr* 1964; **16**: 51–93.
15. Workman P, Twentyman P, Balkwill F, Balmain A, Chaplin D, Double J, Embleton J, Newell D, Raymond R, Stables J, Stephens T, Wallace J. United Kingdom co-ordinating Committee on Cancer Research (UKCCCR) Guidelines for the welfare of animals in experimental neoplasia (second edition). *Br J Cancer* 1998; **77**: 1–10.
16. Murphy ME, Sies H. Visible-range low-level chemiluminescence in biological systems. *Methods Enzymol* 1990; **186**: 595–610.
17. Cadenas E, Boveris A, Chance B. Low-level chemiluminescence of bovine heart submitochondrial particles. *Biochem J* 1980; **186**: 659–67.
18. Howes RM, Steele RH. Microsomal chemiluminescence induced by NADPH and its relation to lipid peroxidation. *Res Commun Chem Pathol Pharmacol* 1971; **2**: 619–26.
19. Vladimilov Yu A, Roshchupkin DI, Fesenko EE. Photochemical reactions in amino acid residues and inactivation of enzymes during UV irradiation. *Photochem Photobiol* 1970; **11**: 227–46.
20. Oberly LW, Spitz DR. Assay of superoxide dismutase activity in tumor tissue. *Methods Enzymol* 1984; **105**: 457–64.

6 ナノセンシングカプセルの医療応用と未来展望

■武田元博 東北大学大学院医学系研究科外科病態学講座
粕谷厚生 東北大学加齢医学研究所
川添良幸 東北大学学際科学研究センター
大内憲明 東北大学大学院医学系研究科外科病態学講座

武田　元博
1987年東北大学医学部医学科卒業。89年東北大学第二外科入局。93年山形県テクノポリス財団主任研究員。2001年東北大学病院乳腺分泌外科助手。
研究テーマは乳腺外科，ナノテクノロジー，生物フォトン現象。趣味は登山，車いじり，料理。

Key words: nano-sized sensing capsules, fullerene,Oligo-dendrimer, silicone nano-cluster peptide-nano carrier

Abstract

近年のナノテクノロジーの進歩は医療に影響を与えつつある。真のナノテクノロジーは従来のマイクロマシーン技術を小さくすることではなく、分子設計に基づき、原子から新たな分子・物質を創造することである。例えば従来存在しないと考えられてきたフラーレンタイプのシリコンクラスターは、2001年Kawazoeらにより安定な構造を取り得ることが初めて予測された。その翌年Oharaらによりその存在が実証され、その蛍光特性から新たな医療応用が期待される。このように新たな物質が次々に創生されつつあり、医療技術に大きな変化をもたらすと考えられる。

はじめに

現在，シリコン加工技術はサブミクロンレベルに達し，最近ではさらに小さなレベルでの制御技術による新た物質の創生が注目されている。これは，従来のサイズを小さくして行く技術ではなく，原子·分子の特性を基礎とし，その組合せによって，指先に乗るチップ中に図書館全体の所蔵物を書き込めるような超高密度デバイスなどを実現する技術といい換えることができる。ナノテクノロジーは，このように未だ実現していないナノメートルレベルの物質を扱う，将来飛躍的に発展するであろう高度医療技術社会に対応していくための技術でもある。ナノテクノロジーによって創生された物質としてカーボンフラーレン，シリコンフラーレンなどが挙げられるが，この創生には近年のコンピュータサイエンスの飛躍的な発展が大きく関与している。すなわちクーロン相互作用する電子と原子核からなる多体系に対する量子力学の方程式を数値的に解く，第一原理計算と呼ばれるスーパーコンピュータを用いたシミュレーションにより，実験以前に新物質の構造と物性を予言するなどの技術が急速に発展した。コンピュータサイエンスの発展の結果，従来予測し得なかった構造・物理的性質を持つ分子やクラスター構造が今後次々と予測・作製されると考えられる。本稿では近年実用化しつつある，機能性クラスター＝ナノディバイスの医療応用について解説する。

1. ナノクラスター

近年，分子レベルで有用な機能を備えるさまざまな構造が発見され，その応用が始まっ

Medical Application and Future Innovation of Nano-sized Sensing Capsules: Motohiro Takeda, Noriaki Ohuchi, Graduate School of Medicine, Tohoku University,Kousei Kasuya, Institute for Differentiation, Aging and Cancer, Tohoku University, Yoshiyuki Kawazoe, Center for Interdisciplinary Research, Tohoku University

ている。以下に述べるナノクラスターはそれぞれが単体として蛍光マーカーとしての機能を有するものがあり，これらは表面の修飾により分子キャリアーとして drug derivery system(DDS)としても利用可能である。ナノクラスターはDDSなどの治療のみならず，分子マーカー，造影剤，センチネルリンパ節マーカーなど診断への利用も期待される。

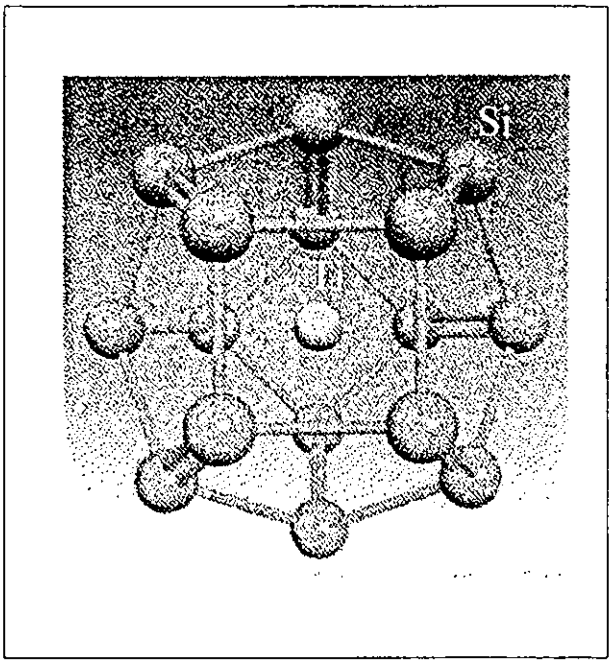

図1　金属内包シリコンフラーレンの一例

1）カーボンフラーレン，カーボンナノチューブ

すでに広く知られているが，カーボンクラスターの1種である，カーボンフラーレンネットワークのとる構造としては，これまでC60，C70のサッカーボール構造（直径およそ1nm）と，ネットワークが円錐・円筒状（直径数nm）になった構造の2種類が知られてい

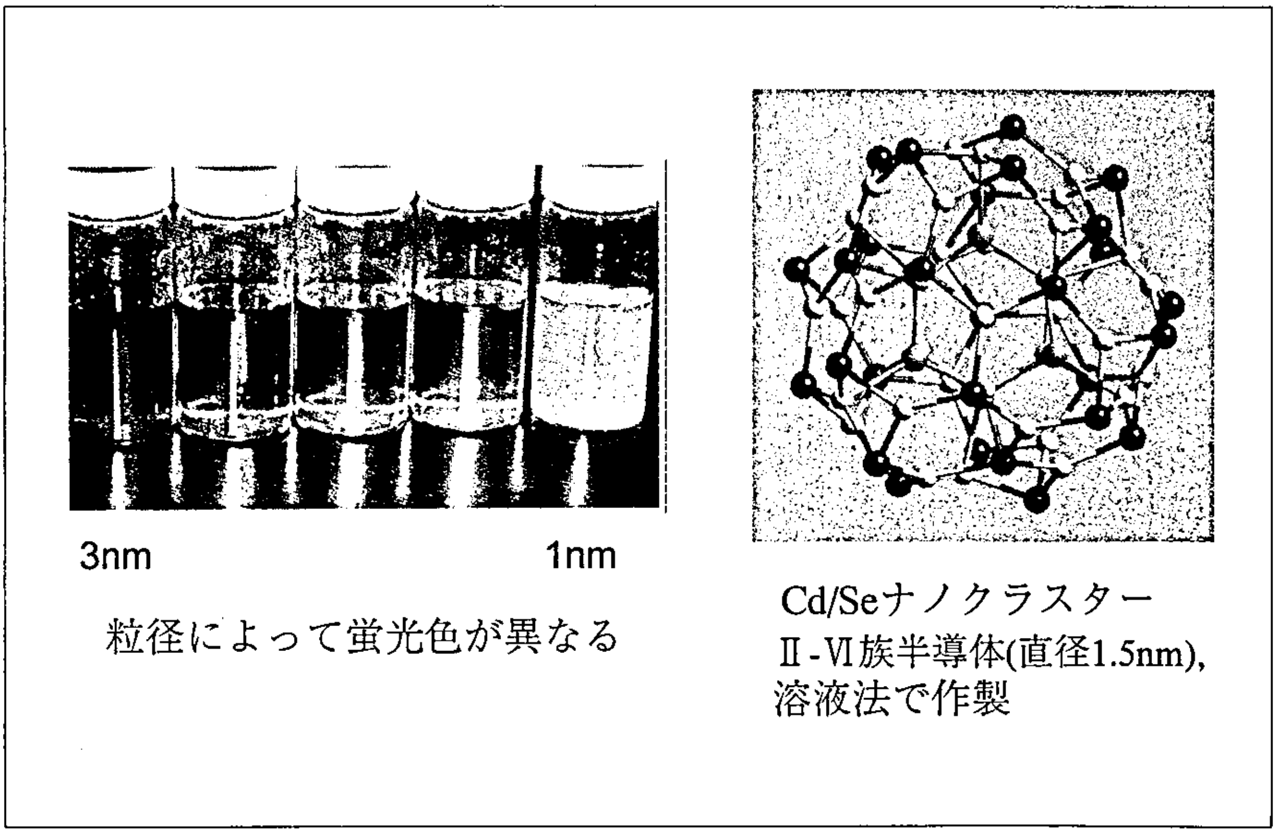

図2　Cd/Seナノクラスターと粒経調節による色調の変化

て，C60，C70は1985年にKroto・Smalley，カーボンナノチューブは1991年にIijimaらによって発見された。

Krotoらはフラーレン発見時に様々な原子の内包化により多様な応用が期待できること，実際に酸素原子やランタン原子が内包できることについて述べているが，その後，ベリリウム等金属原子を内包できることが証明された。そしてこの結果を基に新たな応用を視野に入れた研究が展開されつつある。現在のところ，ボーリングボールやエンジンオイルの添加剤などへの利用にとどまっているが，近年表面の修飾による親水化も実現し，DDSのキャリアー等，応用の拡大が期待される。

カーボンナノチューブは単層もしくは渦巻状の角型のフラーレンネットワークである。現在，原子間力顕微鏡の先端チップに利用され，その性能を飛躍的に向上させた。原子間力顕微鏡の分解能は数nmに達している。カーボンナノチューブも今後，もっとも細い導電ケーブルとしてナノエレクトロニクスを始めとした医療応用が期待されるナノクラスターの一つである。

2）シリコンナノクラスター

従来，シリコンには，十量体以上で対称性のよいクラスターは存在しないとされてきた。2001年に川添らの第一原理に基づくスーパーコンピューターを用いた計算によって，金属原子を内包させると，フラーレン型の極めて対称性のよいクラスターが精製できることがKumar，Kawazoeらによって理論的に初めて示された（図1）。

そして2002年には早くもその存在が実験的にOhara，Nakajimaらによって実証された。カーボンフラーレン同様，安定なケージ構造を取っていることから安定と考えられ，蛍光マーカーとしての性質も持つことから今後，幅広い応用が期待される。

3）量子ドット

カドミウム（Cd）とセレナイド（Se）等，Ⅳ族とⅤ族の元素の組み合わせによるこの半導体クラスター（直径2-10nm）は，従来の蛍光色素にない3つの優れた蛍光特性をもつ。

①従来の蛍光色素が特定波長の光を吸収して励起され，特定波長の蛍光を放出するのに比べ，QDはある一定波長以上の光エネルギーはすべて吸収して励起状態になり，基底状態に戻る時は単一波長の蛍光のみ発する。そのため励起効率が極めて高く，従来の蛍光色素の20-30倍に達する。

②材料が無機物であるため有機系の蛍光色素に比べ，極めて高い耐光性を有する。従って繰り返しの励起光照射に耐える。

③同じ材料でも粒径を変えるだけで蛍光波長を自在に変化させることが可能である（図2）。従って同一材料で蛍光波長の異なる粒子を作ることができる。

既にQuantum Dot社からQuantum Dot (QD)が昨年から市販され，さらにさまざまなタイプのQDが各国で開発されている。新たな蛍光マーカーとして様々な角度からの応用が期待されている。

4）オリゴデンドリマー

これは有機デンドリマーと呼ばれ、多数の枝が球から突き出た，いがぐり状を呈するその特異な構造から医療応用，特にDDSの担体としての利用が期待される物質の一つであ

る。サイズはタンパク質とほぼ同等である。特色としては外界との接触面積が非常に大きく，デンドリマーの枝々の間には莫大な空間が存在するため，その間に薬剤を内包させれば，病変部までの薬剤担体として利用可能となる。

5）ペプチドナノキャリアー

キトサンのデオキシコール酸添加による疏水化・ミセルの形成，亜硝酸ナトリウム添加による凝集・解離を利用してサイズ・形状をコントロールできる（径およそ130-300nm）ことからペプチド，薬物，遺伝子などの担体としての利用が期待される。

2. まとめ

ナノテクノロジーは現在急速に発展しつつあるが，特に医療への応用に際しては体内動態等，安全性の確保が必須である。

しかしこのような問題も乗り越え，今後さらに大きく進歩し，ゲノム科学がそうであるように，ナノテクノロジー科学を治療に生かす手段として医学における主要な研究分野となり，かつ大きな産業分野として成長すると考えられる。

〈BIO Information〉

文部科学省ナノテクノロジー総合支援プロジェクト
第2回分野横断スクール「ナノバイオスクール」プログラム

独立行政法人物質・材料研究機構は第2回分野横断スクール「ナノバイオスクール」を開催します。

主催:　独立行政法人物質・材料研究機構　ナノテクノロジー総合支援プロジェクトセンター
開催日程: 平成17年1月17日(月)10:00開講、18日(火)17:00終了
開催場所: 虎ノ門パストラル　(東京都港区虎ノ門4-1-1. Tel:03-3432-7261(代) http://www.pastoral.or.jp/)

第1日 1月17日(月):生命の仕組みと運動に学ぶナノテクノロジー
1)　開会の挨拶　文部科学省研究振興局 基礎基盤研究課
2)　開講の挨拶　大阪大学 教授 柳田 敏雄
3)　「生命の仕組みを一分子ごとに追跡する」　大阪大学 教授 柳田 敏雄
4)　「超分子ナノマシンの自己構築とスイッチ機構」　大阪大学 教授 難波 啓一
5)　「回転分子モーター」　東京大学 助教授 野地 博行

第2日 1月18日(火):生命における発生機構と情報伝達に学ぶ
6)　「脳の分節構造にもとづくニューロンの機能分化と機能結合」　大阪大学 助教授 小田 洋一
7)　「生命におけるパターン形成のしくみ」　名古屋大学 教授 近藤 滋
8)　「ゲノムバイオロジーとナノバイオテクノロジーの融合」　かずさDNA研究所部長 小原 収
9)　Closing Remarks　東京大学 教授 榊 裕之

応募方法:当センターのフォームよりお申込みください。
お問い合わせ先：独立行政法人物質・材料研究機構 ナノテクノロジー総合支援プロジェクトセンター
岡村 茂 (電話 03-5404-3286)、 鈴木 敦 (電話 03-5404-3282)
独立行政法人物質・材料研究機構　広報室 (電話 029-859-2026)

The EMBO Journal (2004) 23, 2993–2999 | © 2004 European Molecular Biology Organization | All Rights Reserved 0261-4189/04
www.embojournal.org

THE
EMBO
JOURNAL

Rapid double 8-nm steps by a kinesin mutant

Hideo Higuchi[1], Christian Eric Bronner[2], Hee-Won Park[3] and Sharyn A Endow[2,*]

[1]Department of Metallurgy and Center for Interdisciplinary Research, Tohoku University, Sendai, Japan, [2]Department of Cell Biology, Duke University Medical Center, Durham, NC, USA and [3]Department of Structural Biology, St Jude Children's Research Hospital, Memphis, TN, USA

The mechanism by which conventional kinesin walks along microtubules is poorly understood, but may involve alternate binding to the microtubule and hydrolysis of ATP by the two heads. Here we report a single amino-acid change that affects stepping by the motor. Under low force or low ATP concentration, the motor moves by successive 8-nm steps in single-motor laser-trap assays, indicating that the mutation does not alter the basic mechanism of kinesin walking. Remarkably, under high force, the mutant motor takes successive 16-nm displacements that can be resolved into rapid double 8-nm steps with a short dwell between steps, followed by a longer dwell. The alternating short and long dwells under high force demonstrate that the motor stepping mechanism is inherently asymmetric, revealing an asymmetric phase in the kinesin walking cycle. Our findings support an asymmetric two-headed walking model for kinesin, with cooperative interactions between the two heads. The sensitivity of the 16-nm displacements to nucleotide and load raises the possibility that ADP release is a force-producing event of the kinesin cycle.

The EMBO Journal (2004) 23, 2993–2999. doi:10.1038/sj.emboj.7600306; Published online 15 July 2004
Subject Categories: membranes & transport; cell & tissue architecture
Keywords: double steps; kinesin; motor mutant; stepping mechanism

Introduction

The kinesin motor proteins bind to ATP and microtubules, and use the energy of nucleotide hydrolysis to move along the microtubule. The first discovered or conventional kinesin is a highly processive motor that takes more than a hundred steps each time it binds to a microtubule (Howard *et al*, 1989; Svoboda *et al*, 1993; Hackney, 1995). Steps by conventional kinesin along a microtubule are tightly coupled to ATP hydrolysis—the motor takes a single 8-nm step for each ATP it hydrolyzes (Schnitzer and Block, 1997; Coy *et al*, 1999).

The mechanism by which kinesin walks along a microtubule is not well understood, although several models have been postulated. One model involves a hand-over-hand stepping mechanism in which the two heads of the motor alternate in binding to the microtubule and hydrolyzing ATP, each head in turn taking a step to advance the motor towards the microtubule plus end (Howard, 2001; Schief and Howard, 2001). This model is supported by the finding that processivity of kinesin requires two heads (Hancock and Howard, 1998). It accounts for the observed cooperativity of binding to nucleotide and microtubules by the two heads of kinesin—the finding that only one head of the dimeric motor binds to a microtubule and releases ADP in the absence of ATP, and that ATP hydrolysis by the bound head is required for the other head to bind to the microtubule (Hackney, 1994)—by postulating that both heads participate in ATP hydrolysis in an alternating manner. If both heads hydrolyze ATP, the tight coupling between ATP hydrolysis and steps by the motor requires that both heads be involved in producing force and taking steps along the microtubule.

A hand-over-hand model could involve either a symmetric mechanism in which the rear head always steps to the same side of the forward head to take the next step along the microtubule (Howard, 1996), or an asymmetric mechanism in which the rear head steps to either side of the forward head (Hirose *et al*, 2000; Hoenger *et al*, 2000; Schliwa, 2003). The rationale underlying the proposal of a symmetric hand-over-hand mechanism is that the two heads of the dimeric motor are functionally equivalent and should undergo the same movements and conformational changes during the nucleotide hydrolysis cycle (Howard, 1996). The only available crystal structure of dimeric kinesin shows a rotational symmetry of the two heads around the axis of the coiled-coil stalk that causes the microtubule-binding regions of the heads to be on opposite sides of the motor (Kozielski *et al*, 1997). Thus, a symmetric hand-over-hand model would require that the motor rotate ~180° each time an unbound head binds to the microtubule to take a step. This should produce rotations during processive movement that are detectable experimentally.

Failure to observe the rotational movement predicted by a hand-over-hand mechanism has led to the proposal of an 'inchworm' model in which only one head binds to the microtubule and hydrolyzes ATP, dragging the second head along (Hua *et al*, 2002). This model is consistent with the failure to observe 180° rotations of microtubules bound to single kinesin motors, but does not account for the cooperativity of nucleotide and microtubule binding by the two heads of the motor (Hackney, 1994), which requires that both heads of the motor hydrolyze ATP and produce force. Further, the experimental results do not compel an inchworm model, as they could also be accounted for by an asymmetric hand-over-hand model in which conformational changes of the neck linker or another structural element, together with stepping by the rear head to either side of the forward head in successive steps, produce net rotations too small to be detected in the previous experiments (Hua *et al*, 2002).

Here we report a single amino-acid change of conventional kinesin that affects stepping by the motor. The mutant motor

---

*Corresponding author. Department of Cell Biology, Duke University Medical Center, 438 Jones Building, Research Drive, Durham, NC 27710, USA. Tel.: +1 919 684 4311; Fax: +1 919 684 8090;
E-mail: endow@duke.edu

Received: 24 March 2004; accepted: 11 June 2004; published online: 15 July 2004

moves processively along the microtubule by taking successive 8-nm steps, like wild-type kinesin, but under high force the motor moves by 16-nm displacements instead of 8-nm steps. Analysis of the 16-nm displacements reveals that the motor stepping mechanism is asymmetric. The asymmetry is not stochastic, but recurs in a regular pattern that compels an asymmetric mechanism for kinesin walking. The load sensitivity of the 16-nm displacements identifies a potential force-producing event of the kinesin cycle.

Results

Mutant design

The kinesin-T94S mutant was designed to make the highly conserved nucleotide-binding motif or P-loop of *Drosophila* kinesin heavy chain, GQTSSGKT, resemble more closely the P-loop of the myosins, GESGAGKT, in amino-acid sequence. The change of T94 to S causes only a small predicted structural change in the motor (Figure 1); however, T94 interacts with the β-phosphate of ADP in the kinesin motors and may help stabilize ADP binding. The point mutation was thus expected to open the nucleotide-binding cleft and permit more rapid nucleotide binding or release by the motor. The mutant motor was expressed in bacteria as a fusion to a biotin-binding protein and tested for ADP release in biochemical assays and velocity of movement along microtubules in *in vitro* motility assays.

ADP release assays

Single-turnover mant-ADP release experiments using FPLC-purified mutant or wild-type motor protein without microtubules showed that, upon addition of 500 μM Mg·ATP, the kinesin-T94S mutant releases ADP ~3.6-fold faster ($0.0128\pm0.0013\,s^{-1}$, $n=11$) than wild-type kinesin ($0.00353\pm0.00017\,s^{-1}$, $n=12$) (Table I). When no nucleotide was added, the mutant motor released ADP at the same rate ($0.00319\pm0.00079\,s^{-1}$, $n=4$) as the wild-type motor with added Mg·ATP, indicating that release of ADP by the kinesin-T94S motor is not dependent on binding of ATP or microtubules. The wild-type motor without added nucleotide released ADP more slowly ($0.00154\pm0.00080\,s^{-1}$, $n=3$), with poorer curve fits (linear correlation coefficient, $R>0.75$) than the kinesin-T94S mutant ($R>0.95$).

Single-turnover assays with microtubules were performed by mixing 0.2 μM kinesin-T94S or wild-type kinesin with 1 μM microtubules and monitoring the release of mant-ADP in a fluorometer. Results of these assays showed an acceleration of ADP release by microtubules (9- to 10-fold), which was comparable for the mutant and wild type. The dissociation rate for the kinesin-T94S motor ($0.0287\pm0.0187\,s^{-1}$, $n=9$) was higher than that of wild-type kinesin ($0.0162\pm0.0062\,s^{-1}$, $n=8$) (Table I), but the overall values did not differ significantly due to the variability from assay to assay. Attempts to measure the k_{cat} of the mutant and wild-type motors in ATPase assays with microtubules gave variable values that were lower than normal for wild type and somewhat higher for the mutant. The high variability in mant-ADP release rates in the presence of microtubules and microtubule-stimulated k_{cat} values may be due to the effects of the BIO fusion protein on motor–microtubule interactions when the motor is not bound to a glass surface or bead, as motor velocities in gliding and laser-trap assays were in the normal range for wild-type kinesin (see below). The k_{cat} values with microtubules are not reported here to avoid misinterpretation of the mutant effects. Detailed studies of nonfusion mutant and wild-type motors in the presence of

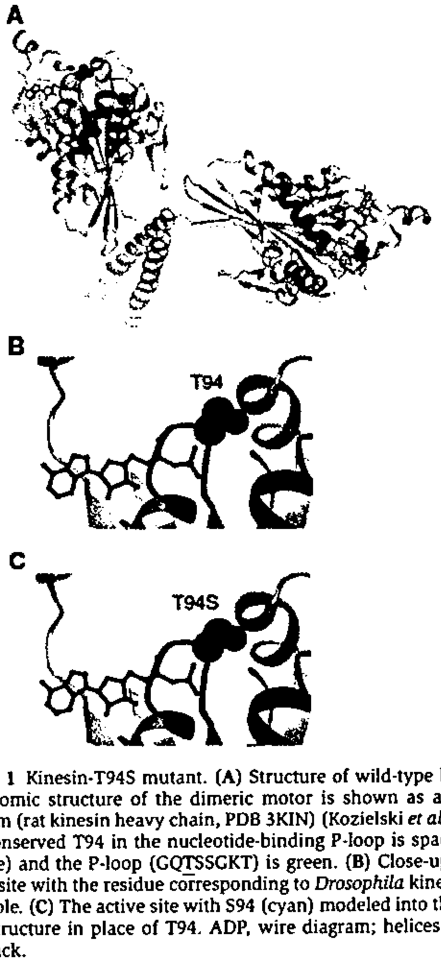

Figure 1 Kinesin-T94S mutant. (**A**) Structure of wild-type kinesin. The atomic structure of the dimeric motor is shown as a ribbon diagram (rat kinesin heavy chain, PDB 3KIN) (Kozielski *et al*, 1997). The conserved T94 in the nucleotide-binding P-loop is space-filled (purple) and the P-loop (GQTSSGKT) is green. (**B**) Close-up of the active site with the residue corresponding to *Drosophila* kinesin T94 in purple. (**C**) The active site with S94 (cyan) modeled into the wild-type structure in place of T94. ADP, wire diagram; helices α4 and α5, black.

Table I Kinetic properties of the kinesin-T94S and wild-type kinesin motors

	Kinesin-T94S	Wild-type kinesin
k_d, ADP release−ATP	$0.00319\pm0.00079\,s^{-1}$, $n=4$, $R>0.95$	$0.00154\pm0.00080\,s^{-1}$, $n=3$, $R>0.75$
k_d, ADP release+ATP	$0.0128\pm0.0013\,s^{-1}$, $n=11$, $R\geqslant0.90$	$0.00353\pm0.00017\,s^{-1}$, $n=12$, $R>0.93$
k_d, ADP release+MTs	$0.0287\pm0.0187\,s^{-1}$, $n=9$, $R\geqslant0.73$	$0.0162\pm0.0062\,s^{-1}$, $n=8$, $R\geqslant0.65$
Velocity, MT gliding	255 ± 13 nm/s, $n=20$	853 ± 25 nm/s, $n=19$

Values are the mean ± s.e.m.; *R*, linear correlation coefficient for the curve fit (values closer to 1.00 indicate a better fit); MT, microtubules.

microtubules will be required to determine the effects of the T94S mutation on motor binding to nucleotide in the presence of microtubules. The altered rate of ADP release by the kinesin-T94S mutant in the absence of microtubules and the initial data presented here for assays with microtubules raise the possibility that ADP release in the presence of microtubules is also altered.

Gliding assays

Microtubule gliding assays (Song *et al*, 1997) were performed with lysates of the kinesin-T94S or wild-type motor. The assays showed good binding to microtubules by the motors attached to the coverslip, but a slower gliding velocity by ~3.3-fold for the mutant (255±13 nm/s, $n=20$) compared to wild type (853±25 nm/s, $n=19$) (Table I).

Laser-trap assays

The increased ADP release rate in the absence of microtubules, but decreased velocity in gliding assays, suggested that stepping of the kinesin-T94S mutant along microtubules might be altered. Traces of single kinesin-T94S motors in laser-trap assays showed slow movement compared to wild type (Figure 2A and B). The velocity of the mutant at low load (~1 pN) was 250 nm/s, which was about one-third the velocity of wild type, 760 nm/s, consistent with the gliding assays. The stall force of ~8 pN for the mutant was similar to

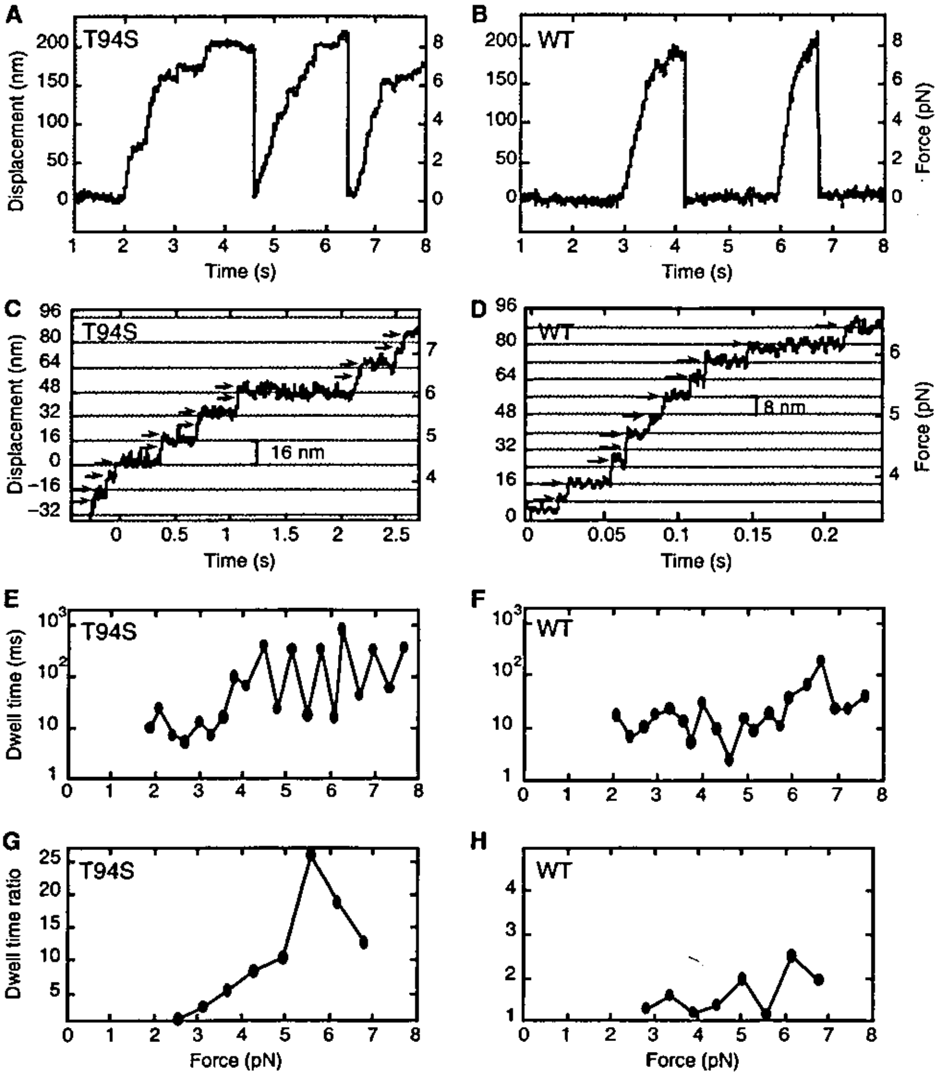

Figure 2 Single-molecule laser-trap assays of kinesin-T94S and wild-type kinesin. (**A, B**) The traces show processive movement by single kinesin-T94S (magenta) and wild-type kinesin (green) motors. (**C, D**) Single kinesin-T94S motors showed successive 8-nm steps at forces < ~4 pN, but exhibited successive 16-nm displacements, consisting of rapid double 8-nm steps, at forces > ~4 pN. Single wild-type kinesin motors under the same conditions showed sequential 8-nm steps. (**E, F**) A plot of dwell time versus force shows alternating short and long dwells following sequential 8-nm steps by the kinesin-T94S mutant. The wild type shows variable dwells following sequential 8-nm steps. (**G, H**) The ratios of the long dwell times divided by the short dwell times at different forces, calculated by averaging overlapping sets of three successive odd and even steps (see Materials and methods) corresponding to the traces in (C, D). The dwell time ratios or limp factors L of the mutant are significantly greater than those of wild type at forces > ~4 pN. Note the difference in Y-axis scales in (C, H).

wild type. The mutant was processive with a step size of 8 nm at low load (< ~4 pN) (Figure 2C). Remarkably, at high load, the mutant showed frequent 16-nm displacements, which could be resolved into two rapid 8-nm steps with a short dwell between steps followed by a longer dwell, with the short and long dwells alternating between successive 8-nm steps (Figure 2C and E). The wild-type motor showed 8-nm steps, as reported by others (Svoboda *et al*, 1993; Nishiyama *et al*, 2002), with variable dwells between steps (Figure 2D and F).

The dwell times between steps by the mutant and wild-type motors were analyzed statistically. Steps in traces were assigned as odd or even, and the dwell times for three sequential odd steps and three sequential even steps were averaged (total = 6 steps). The longer mean dwell time was divided by the shorter one to obtain the ratio. Two steps were then slipped from the first step, the next dwell time ratio was calculated, and this process was reiterated for the length of the run. Analysis of the traces for the mutant and wild type in Figure 2C and D is shown in Figure 2G and H.

In all, 31 traces of the mutant and 20 traces of wild type were analyzed in this way without selecting for 8- or 16-nm displacements (Figure 3). The dwell time ratio, referred to as the limp factor L (Asbury *et al*, 2003), increased sharply for the mutant from 2.99 to 6.35 with 2.4–6.9 pN force (Figure 3A). By contrast, the limp factor of wild-type kinesin increased slowly from 1.88 to 2.57 with 2.4–6.7 pN force, remaining at a low ratio of <3 (Figure 3A).

The average dwell time of the kinesin-T94S mutant was ~2.5 times longer than that of wild type (mutant = 37 ms and wild type = 14.6 ms at 2.4 pN; mutant = 159 ms and wild type = 61 ms at 6.7–6.9 pN) (Figure 3B and C). For the mutant, the long dwell times increased sharply with force, whereas the short dwell times increased more gradually. The short dwell times of the mutant were longer than the average dwell times of wild type at low force, but they were shorter at high force.

The 16-nm displacements, characterized by short dwell times and high L values, appeared clearly at high force (⩾4 pN), where they were observed frequently for single kinesin-T94S motors ($L>5$, 32% of dwell time ratios, total = 149, compared to 22% at <4 pN, total = 74). The 16-nm displacements were observed infrequently for wild type (2% of dwell time ratios, total = 148).

At low force, single kinesin-T94S motors showed 8-nm steps at higher frequency than at high force, rather than 16-nm displacements. The appearance of the 16-nm displacements at high force indicates the existence of a phase in the kinesin-T94S walking cycle that can be accelerated by force, resulting in the rapid double 8-nm steps. The 8-nm steps by the mutant were also observed at low ATP concentration (10 μM) ($L = 2.37$ at 2.3–6.2 pN force). The low frequency of 16-nm displacements by the mutant at low ATP concentration ($L>5$, 5% of dwell times, total = 99) is probably due to the time required to release ADP and bind ATP. The rate-limiting step of the kinesin cycle is thought to be the release of ADP (Hackney, 1988). But because the dwell time for the mutant at 10 μM ATP was ~3 times that at 1 mM ATP, the rate-limiting step at low ATP concentration is likely to be ATP binding rather than ADP release, making the dwell time between steps by the mutant close to that of wild type.

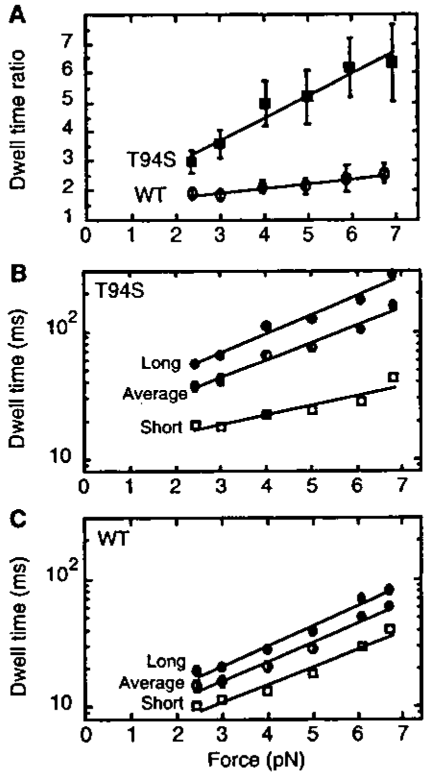

Figure 3 Dwell times versus force for steps by kinesin-T94S and wild-type kinesin. (**A**) The dwell time ratio or limp factor for 8-nm steps by the kinesin-T94S mutant (magenta) or wild-type kinesin (green) increases linearly with force, but the increase is significantly greater for the mutant than wild type. (**B**) The increase in long dwell times of the mutant with increasing force is paralleled by the increase in the average dwell times, while the short dwell times increase more slowly. (**C**) The long and short dwell times of wild-type increase in parallel with one another and with the average dwell times with increasing force. The error bars show the standard error of the mean (s.e.m.) for the dwell time ratios and average dwell times.

Discussion

A kinesin stepping mutant

We report here a new mutant of *Drosophila* kinesin heavy chain that was rationally designed to make the nucleotide-binding P-loop resemble more closely that of the myosins. The mutant motor has a change of T94S in the P-loop, which was expected to open the nucleotide-binding cleft and increase the rate of nucleotide binding or release by the motor. This relatively minor structural change causes the motor to release ADP ~3.6-fold faster than wild type in the absence of microtubules and to translocate microtubules in gliding assays with a velocity ~3.3-fold slower than wild type. In single-molecule laser-trap assays, the mutant motor shows frequent 16-nm displacements under high force, which are resolvable into rapid double 8-nm steps, consisting of alternating slow and fast steps. At low force or low ATP concentration, successive 8-nm steps were observed instead of 16-nm displacements. The wild-type motor showed infrequent 16-nm displacements due to rapid double 8-nm steps.

The frequency of rapid double 8-nm steps is thus enhanced in the mutant compared to wild type.

The 16-nm displacements arise by alternating fast and slow dwell times, causing alternate steps to be fast and slow. The structural basis of a slow step by the kinesin-T94S mutant that alternates with a fast step could be due to an inherent asymmetry of stepping to the right or left of the forward head caused by the handedness of the twist of the coiled coil. Stepping to the right might be constrained by the twist of the coiled coil, whereas stepping to the left might not be, and might be accelerated by interactions of the rear head with the forward head.

The successive 16-nm displacements in the kinesin-T94S traces with alternating short and long dwell times indicate that a step in the kinesin walking cycle is asymmetric, as predicted by asymmetric two-headed walking models, but not by symmetric ones such as hand-over-hand models in which the rear head always steps to the same side of the forward head (Howard, 1996), or inchworm models, in which only one head steps, dragging the other head along (Hua *et al*, 2002). Our results favor an asymmetric walking model in which the two heads of kinesin alternate in binding to the microtubule and hydrolyzing ATP.

Stepping by heterodimeric kinesin

Recently, others have reported 16-nm displacements by a heterodimeric kinesin protein consisting of kinetically different mutant and wild-type motor subunits (Kaseda *et al*, 2003), providing evidence that the two heads of the heterodimeric motor alternate in stepping. The interactions of the two heads of a heterodimeric motor with one another could differ from that of the native motor, however, due to the mutation in one head or due to the different proteins to which they were fused. The results we report here differ from those of Kaseda *et al* (2003) in that we observe asymmetry of movement for a homodimeric kinesin motor. This substantiates these previous findings by showing that the asymmetric steps of the heterodimer must have been due to an inherent asymmetry of stepping by the motor and were not dependent on the differences in the motor subunits.

Limping by wild-type kinesin motors

Our findings differ from those reported recently by others (Asbury *et al*, 2003) for wild-type *Drosophila* and native squid kinesin. These workers found evidence for alternating slow and fast steps under high force (4 pN) for truncated *Drosophila* kinesin proteins, whereas we did not observe frequent 16-nm displacements for our truncated wild-type kinesin, which was expressed as a fusion to a 106-residue BIO protein with two linker residues. The basis of these conflicting results could be a difference in the kinesin preparations used in the assays, a dependence of limping on the total length of the proteins analyzed, such that shorter proteins show a greater tendency to limp because they interact asymmetrically with the surface of the bead rather than the microtubule, or the conditions of the laser-trap assays. In the present work, we used a kinesin motor fused to a BIO domain to prevent interactions of the motor with the bead.

The velocities reported by Asbury *et al* (2003) both for their truncated and native kinesin proteins were unusually slow, ~65–165 nm/s (calculated from the mean fast and slow dwell times in their Figure 3C). These velocities are significantly slower than the velocities of 300 and ~600 nm/s for squid kinesin at 4 pN reported previously by the same laboratory (Visscher *et al*, 1999; Block *et al*, 2003), and the velocity of 390 nm/s at 4.0 pN of our wild-type kinesin, DmK447-BIO. These unusually slow velocities could arise if the force-clamp assays were performed under higher actual force than the reported value of 4 pN, or the kinesin proteins used in the assays were heterogeneous, comprising some motors in which one head was slower than the other due to partial inactivation during purification. The slow velocities of the truncated and native kinesin motors reported by Asbury *et al* (2003) need to be accounted for and correlated with the limping behavior of the motors before attempting to reconcile our data with theirs.

Kinesin-T94S and stepping models

The results we report here are important in that they show that a kinesin mutant with a single amino-acid change in the nucleotide-binding P-loop, under high force, shows a high frequency of rapid double 8-nm steps, resulting in 16-nm displacements. Under low force or low ATP concentrations, the mutant takes 8-nm steps, like wild-type kinesin. This suggests that the mutation enhances a step in the wild-type kinesin stepping cycle that is sensitive to load and the nucleotide state of the motor. Load-sensitive conformational changes have not previously been identified for kinesin and are believed to correspond to the force-producing steps of the hydrolysis cycle. The finding that the mutant motor is altered in ADP release tentatively identifies ADP release as a force-generating event of the kinesin cycle, although it is still possible that a different step of the hydrolysis cycle is affected. Further biochemical studies will be required to determine the step in the cycle that is altered in the mutant and how it affects the motor stepping mechanism. The observation of rapid double 8-nm steps under high load with alternating long and short dwells implies that a phase of the stepping cycle is affected by the mutant that involves the alternative regulation or interactions of the two heads.

The disappearance of the 16-nm displacements at low force or low ATP concentration indicate that another rate-limiting step, probably ATP binding, suppresses the rapid double 8-nm steps by interposing a longer dwell between the steps, resolving them into two steps. The ability of the kinesin-T94S motor to take successive 8-nm steps demonstrates that the basic mechanism of walking by the kinesin motor is unaltered. The appearance of the rapid double 8-nm steps or 16-nm displacements at high force and their infrequent appearance in wild-type traces indicates that the mutant enhances a step in the walking cycle that is inherently asymmetric, revealing an asymmetric walking mechanism for kinesin.

Materials and methods

Plasmids

Plasmids to express the kinesin-T94S mutant or corresponding wild-type *Drosophila* kinesin heavy chain (KHC) motor fused to a biotin-binding protein were constructed by inserting DNA fragments synthesized by the polymerase chain reaction (PCR) into *pMW172/KHC* (Song and Endow, 1996). The plasmids encode M-G-S + KHC residues E4-Q447, linked by G-S to 106 residues of the *Propionibacterium shermanii* biotin-binding transcarboxylase (BIO)

(Pinpoint Xa, Promega). PCR-synthesized regions were confirmed by DNA sequence analysis.

Protein expression and purification

The kinesin-T94S and corresponding wild-type kinesin proteins fused to BIO were expressed in bacteria using the T7 RNA polymerase system (Studier *et al*, 1990). The fusion proteins were 123.4 kDa dimers of a 567-residue subunit. The kinesin region of the fusion protein corresponds to the conserved motor domain (E4-F326), the neck linker (G327-T344) and 103 residues of the coiled coil (A345-Q447). Proteins were purified for biochemical assays by chromatography on P11 phosphocellulose, followed by MonoQ and/or Superose 12 FPLC. The Superose 12 chromatography step was necessary to remove high-molecular-weight kinesin aggregates. The purified proteins were diluted extensively for use in laser-trap assays.

Motility assays

Microtubule gliding assays on motor-coated coverslips were performed as described (Song *et al*, 1997), using lysates of the kinesin-T94S or wild-type motors fused to BIO.

ADP release assays

Single-turnover mant-ADP release experiments were performed using FPLC-purified kinesin-T94S or wild-type protein fused to BIO by incubating 2 μM mant-ATP [2′(3′)-*O*-(*N*-methyl-anthraniloyl)-adenine 5′-triphosphate] with 0.5 μM motor for ⩾2 h on ice in the dark. Samples were warmed to room temperature for 5–10 min and fluorescence (excitation, 356 nm; emission, 446 nm) was recorded in a SPEX FluoroMax or SLM Aminco 8100 spectrofluorometer before and after addition of 500 μM ATP. Mant-ADP release assays in the presence of microtubules were performed by mixing 0.2 μM motor + mant-ATP after incubation on ice with 1 μM GTP-depleted microtubules in a cuvette and recording fluorescence before and after addition of the microtubules. Fluorescence was plotted versus time and data points were fit to a single exponential curve,

$$y = m_3 + m_1 e^{(-m_2 m_0)}$$

where y = fluorescence (cps), m_0 = time (s) and $y = m_3 + m_1$ at $t = 0$, using KaleidaGraph v 3.08d. Dissociation rate constants ($k_d = m_2$) were obtained from the curve fits. In some experiments, samples were spin-dialyzed to remove excess mant-ATP after incubation on ice and before recording fluorescence; rates were the same as assays in which mant-ATP was not depleted. Data for the experiments were therefore combined.

Laser-trap assays

Laser-trap assays were performed using highly diluted purified kinesin-T94S or wild-type motors expressed as fusions to BIO and attached to 0.2 μm avidin-coated beads in buffer + 200 mM NaCl + 1 mM ATP (Endow and Higuchi, 2000; Nishiyama *et al*, 2002). The data were derived from single motors, based on the statistics of binding of the beads to microtubules (Svoboda and Block, 1994; Endow and Higuchi, 2000). Assays performed at low ATP concentrations contained 10 μM ATP. Beads were trapped at a stiffness of 0.04 pN/nm and monitored for binding and movement on microtubules. Data were taken without a low-pass filter, then filtered through 50 Hz (Figure 2A and B) and 200 Hz (Figure 2C and D) low-pass filters for analysis.

Statistical analysis

Dwell times between steps of the mutant and wild type were analyzed statistically, as described by others (Asbury *et al*, 2003). Steps in a given trace were assigned as odd or even, and dwell times of three sequential odd steps and three sequential even steps were averaged. The longer mean dwell time was divided by the shorter one to obtain the dwell time ratio. Two steps were slipped along the trace from the first step, the next dwell time ratio was calculated from the next overlapping six steps, and this process was reiterated for the length of the run. The theoretical ratio for an exponential distribution of random dwell times generated by computer simulation was calculated to be 2.23 for analysis of overlapping sets of six sequential steps and 1.84 for 10 sequential steps. These values were close to the value of 1.79 obtained by analyzing dwell times from computer-simulated stepping records (Asbury *et al*, 2003).

Acknowledgements

We thank C Nicchitta and K Alexander for use of spectrofluorometers, and S Rosenfeld for the gift of mant-ATP. This work was supported by grants from the Japan Ministry of Education, Science, Sport & Culture to HH, Human Frontier Science Program to HH and SAE, St Jude Children's Research Hospital Cancer Center and American Lebanese Syrian Associated Charities to HWP, and NIH to SAE.

References

Asbury CL, Fehr AN, Block SM (2003) Kinesin moves by an asymmetric hand-over-hand mechanism. *Science* **302:** 2130–2134

Block SM, Asbury CL, Shaevitz JW, Lang MJ (2003) Probing the kinesin reaction cycle with a 2D optical force clamp. *Proc Natl Acad Sci USA* **100:** 2351–2356

Coy DL, Wagenbach M, Howard J (1999) Kinesin takes one 8-nm step for each ATP that it hydrolyzes. *J Biol Chem* **274:** 3667–3671

Endow SA, Higuchi H (2000) A mutant of the motor protein kinesin that moves in both directions on microtubules. *Nature* **406:** 913–916

Hackney DD (1988) Kinesin ATPase: rate-limiting ADP release. *Proc Natl Acad Sci USA* **85:** 6314–6318

Hackney DD (1994) Evidence for alternating head catalysis by kinesin during microtubule-stimulated ATP hydrolysis. *Proc Natl Acad Sci USA* **91:** 6865–6869

Hackney DD (1995) Highly processive microtubule-stimulated ATP hydrolysis by dimeric kinesin head domains. *Nature* **377:** 448–450

Hancock WO, Howard J (1998) Processivity of the motor protein kinesin requires two heads. *J Cell Biol* **140:** 1395–1405

Hirose K, Henningsen U, Schliwa M, Toyoshima C, Shimizu T, Alonso M, Cross RA, Amos LA (2000) Structural comparison of dimeric Eg5, Neurospora kinesin (Nkin) and Ncd head-Nkin neck chimera with conventional kinesin. *EMBO J* **19:** 5308–5314

Hoenger A, Thormählen M, Diaz-Avalos R, Doerhoefer M, Goldie KN, Muller J, Mandelkow E (2000) A new look at the microtubule binding patterns of dimeric kinesins. *J Mol Biol* **297:** 1087–1103

Howard J (1996) The movement of kinesin along microtubules. *Ann Rev Physiol* **58:** 703–729

Howard J (2001) *Mechanics of Motor Proteins and the Cytoskeleton*. Sunderland, MA: Sinauer Associates Inc

Howard J, Hudspeth AJ, Vale RD (1989) Movement of microtubules by single kinesin molecules. *Nature* **342:** 154–158

Hua W, Chung J, Gelles J (2002) Distinguishing inchworm and hand-over-hand processive kinesin movement by neck rotation measurements. *Science* **295:** 780–781

Kaseda K, Higuchi H, Hirose K (2003) Alternate fast and slow stepping of a heterodimeric kinesin molecule. *Nat Cell Biol* **5:** 1079–1082

Kozielski F, Sack S, Marx A, Thormählen M, Schönbrunn E, Biou V, Thompson A, Mandelkow E-M, Mandelkow E (1997) The crystal structure of dimeric kinesin and implications for microtubule-dependent motility. *Cell* **91:** 985–994

Nishiyama M, Higuchi H, Yanagida T (2002) Chemomechanical coupling of the forward and backward steps of single kinesin molecules. *Nat Cell Biol* **4:** 790–797

Schief WR, Howard J (2001) Conformational changes during kinesin motility. *Curr Opin Cell Biol* **13:** 19–28

Schliwa M (2003) Kinesin: walking or limping? *Nat Cell Biol* **5:** 1043–1044

Schnitzer MJ, Block SM (1997) Kinesin hydrolyses one ATP per 8-nm step. *Nature* **388:** 386–390